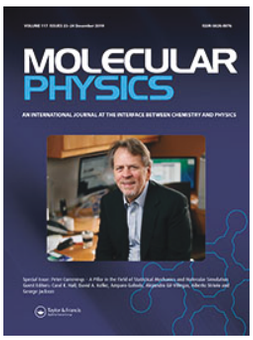

Taylor & Francis
Taylor & Francis Group

Molecular Physics

An International Journal at the Interface Between Chemistry and Physics

ISSN: 0026-8976 (Print) 1362-3028 (Online) Journal homepage: https://www.tandfonline.com/loi/tmph20

Effect of fluorination on the partitioning of alcohols

Mohammad Soroush Barhaghi, Chloe Luyet & Jeffrey J. Potoff

To cite this article: Mohammad Soroush Barhaghi, Chloe Luyet & Jeffrey J. Potoff (2019) Effect of fluorination on the partitioning of alcohols, Molecular Physics, 117:23-24, 3827-3839, DOI: 10.1080/00268976.2019.1669837

To link to this article: https://doi.org/10.1080/00268976.2019.1669837

MOLECULAR PHYSICS
2019, VOL. 117, NOS. 23–24, 3827–3839
https://doi.org/10.1080/00268976.2019.1669837

Taylor & Francis
Taylor & Francis Group

CUMMINGS SPECIAL ISSUE

Effect of fluorination on the partitioning of alcohols

Mohammad Soroush Barhaghi, Chloe Luyet and Jeffrey J. Potoff

Department of Chemical Engineering and Materials Science, Wayne State University, Detroit, MI, USA

ABSTRACT

In order to understand the role of fluorination on the interactions and partitioning of alcohols in aqueous and organic environments, isobaric-isothermal ensemble Monte Carlo simulations are used to determine environmental predictors, such as free energies of hydration and solvation in 1-octanol and n-hexadecane. Calculations are performed with the united-atom Transferable Potentials for Phase Equilibria (TraPPE) force field and compared against available experimental data. TraPPE was found to provide reliable qualitative predictions of trends with respect to the effect of fluorination on partitioning. Investigation of the local solvation environment around the hydroxyl group reveals that fluorination of carbons closest to the hydroxyl group has the greatest effect on solvation free energies for alcohols in water, 1-octanol and n-hexadecane.

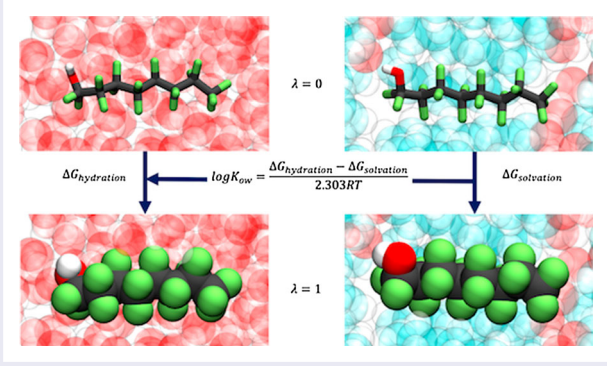

ARTICLE HISTORY
Received 3 July 2019
Accepted 6 September 2019

KEYWORDS
Fluorotelomers; free energy; Monte Carlo; TraPPE

1. Introduction

Perfluoroalkyl substances (PFAS) are a broad class of compounds where fluorine has been substituted for hydrogen on the alkyl chains. The most widely used and industrially relevant PFAS are surfactants, where fluorination of the alkyl tails renders them both hydrophobic and oleophobic, giving rise to unusual properties, such as exceptional chemical and thermal stability and very low interfacial tension at the air–water interface [1–3]. Owing to their unique properties, PFAS are used in a broad array of consumer applications, including coatings for non-stick cookware [4], grease-resistant paper [5], and stain resistant fabrics. Industrial applications include fire-fighting foams [6] and mist-suppressants in hard chrome plating [7].

The strength of the C-F bond, which contributes to the stability of fluorinated surfactants, also makes them extremely resistant to thermal, chemical, or photo degradation; experiments have shown that perfluorinated surfactants are highly resistant to biological degradation [8]. Numerous studies have shown the widespread distribution of PFAS in the environment [9,10]. As a result, PFAS are now considered to be a significant environmental threat [11].

Concerns about the environmental impact of PFAS led to the phase-out of the two most common surfactants, perfluorooctanoic acid (PFOA) and perfluorooctanesulfonate (PFOS); however, the development of new fluorinated surfactants, some with reduced potential for bioaccumulation, is on-going [12,13]. Analysis of fire

CONTACT Jeffrey J. Potoff jpotoff@wayne.edu Department of Chemical Engineering and Materials Science, Wayne State University, Detroit, MI 48202, USA

Supplemental data for this article can be accessed at https://doi.org/10.1080/00268976.2019.1669837

sites where aqueous film forming foams (AFFF) had been used in Ontario, Canada, identified 103 different PFAS [14]. Fast atom bombardment and high resolution quadrupole-time-of-flight mass spectrometry performed on seven AFFF formulations used by the United States Military identified 10 unique classes of compounds, with perfluoroalkyl chain lengths ranging from 4 to 12 carbon atoms [15]. The physicochemical properties, environmental fate, and toxicity of these compounds are largely unknown [15].

Environmental fate models rely on numerous physical property data, two of the most important of which are the Henry's law constant and the octanol–water partition coefficient, $\log K_{ow}$ [16]. Given the breadth of PFAS chemistry and the lack of available experimental data, predictive methods are needed to fill these critical knowledge gaps. Prior work on the partitioning of fluorotelomer alcohols showed that common tools, such as EPISuite [17], CLOGP [18], SPARC [19] and COSMOTherm [20], produce a wide variety of results, with some predictions 2–5 orders of magnitude different than experiment [21].

Alternatively, atomistic computer simulations, combined with free energy methods such as thermodynamic integration [22], free energy perturbation [23,24], or adaptive biasing force [25,26], have been used with great success in the prediction of free energies of hydration and solvation in organic solvents for a wide variety of compounds [27–30]. While most work has focused on applications to drug [31–33] discovery, other calculations have focused on predicting the environmental fate of potentially toxic compounds, such as energetic materials [34,35], ionic liquids [36], and fluorinated alcohols [37]. Additionally, computer simulations provide information on atomic-level structure, supporting the development of structure-property relationships.

While molecular dynamics simulations are widely used for the calculation of free energies of solvation, systems with large energy barriers to configurational and/or conformational change may exhibit biased sampling, leading to incorrect free energies if care is not taken [38]. On the other hand, Monte Carlo simulations allow the system to hop between states and in some cases, may offer conformational sampling advantages over molecular dynamics. Free energies can be determined directly from Gibbs ensemble Monte Carlo simulations from the ratio of number densities of the solute in each phase [39–41]:

$$\Delta G_i^{transfer} = -RT \ln \left(\frac{\left\langle \rho_i^{liquid} \right\rangle}{\left\langle \rho_i^{gas} \right\rangle} \right)_{eq} \quad (1)$$

where R and T are the molar gas constant and absolute temperature in K, respectively, and $\left\langle \rho_i^{liquid} \right\rangle$ and $\left\langle \rho_i^{gas} \right\rangle$ are the ensemble averaged number density (molecule/Å^3) for solute i in liquid and gas phase at equilibrium, respectively.

Gibbs ensemble Monte Carlo provides a straightforward way of determining free energies of transfer as long as a sufficient number of successful exchanges of the solute between phases occurs, which usually requires the use of advanced configurational-bias sampling methods [40–43]. For dense liquids with strong electrostatic interactions, obtaining adequately converged results for certain solutes may be challenging, even with state-of-the-art sampling algorithms for the molecule exchange move. The fluoro-alcohol systems of interest in this work present a perfect storm of sampling problems: the hydroxyl group has strong electrostatic interactions with the solvent (water or octanol) and it is difficult to find a favourably sized cavity to insert the bulky fluorinated alkyl tail. With enough intermediate states, nearly any molecule exchange between phases is possible [44], but if free energies of transfer are the quantity of interest, it may be more effective to perform standard thermodynamic integration or free energy perturbation. Therefore, this work describes the implementation of thermodynamic integration (TI) and free energy perturbation (FEP) methods into the Monte Carlo simulation engine GOMC [45], and the application of TI and FEP to determine the air–water, air-oil, air-octanol, and octanol–water partition coefficients for eight carbon alcohols with varying degrees of fluorination. Partitioning of fluorotelomer alcohols is of interest because they can degrade to form perfluorooctanoic acid (PFOA) [46]. The local solvation structure around C8 alcohols is determined and used to explain the impact of fluorination of the alkyl tail on partitioning.

2. Force field

Calculations were performed using the SPC water model [47], and the Transferable Potentials for Phase Equilibria (TraPPE) force field [48–50] to represent a variety of fluorinated analogues of 1-octanol and n-hexadecane, which are listed in Table 1. All non-bonded force field parameters are listed in Table 2.

In TraPPE, a united-atom representation is used for all CF_x and CH_x groups; i.e. hydrogen or fluorine atoms bonded to carbon atoms are not represented explicitly and are, instead, combined with carbon atoms to form a single interaction site or 'pseudo-atom'. Interactions between pseudo-atoms are described by pairwise-additive 12–6 Lennard-Jones potentials, combined with

Table 1. Fluorinated 1-octanol analogues studied in this work.

Molecular structure	Molecular formula	Molecular name
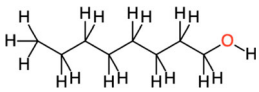	$CH_3(CH_2)_7OH$	H8
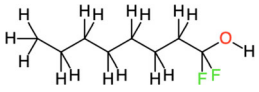	$CH_3(CH_2)_6CF_2OH$	F1H7
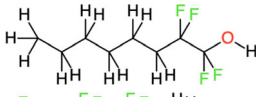	$CH_3(CH_2)_5(CF_2)_2OH$	F2H6
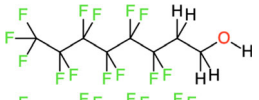	$CF_3(CF_2)_5(CH2)_2OH$	H2F6
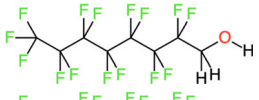	$CF_3(CF_2)_6CH_2OH$	H1F7
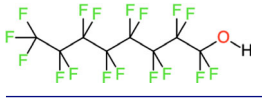	$CF_3(CF_2)_7OH$	F8

Table 2. Non-bonded parameters for alcohols, fluoroalcohols and fluorotelomer alcohols.

Group	ε/k_B (K)	σ (Å)	q_i
	TraPPE-UA		
CH_3	98.0	3.75	0.0/0.265*
CH_2	46.0	3.95	0.0/0.265*
CF_3	87.0	4.36	0.0/0.265*
CF_2	27.5	4.73	0.0/0.265*
O (alcohol)	93.0	3.02	−0.700
H (alcohol)	0.0	0.0	0.435
	SPC		
O	78.21	3.167	−0.820
H	0.0	0.0	0.410

*Partial charges for the C_α bonded to oxygen.

partial charges to represent Coulombic interactions:

$$U_{inter}(r_{ij}) = U_{LJ}(r_{ij}) + U_{Coul}(r_{ij}) \quad (2)$$

$$U_{LJ}(r_{ij}) = 4\varepsilon_{ij}\left[\left(\frac{\sigma_{ij}}{r_{ij}}\right)^{12} - \left(\frac{\sigma_{ij}}{r_{ij}}\right)^{6}\right] \quad (3)$$

$$U_{Coul}(r_{ij}) = \frac{q_i q_j}{4\pi\epsilon_o r_{ij}} \quad (4)$$

where r_{ij}, ε_{ij}, σ_{ij}, q_i, and q_j are the separation, Lennard-Jones well depth, pseudo-atom diameter, and partial charges, respectively, for the pair of interaction sites i and j and ϵ_o is the permittivity of vacuum. Non-bonded parameters for alkyl [48], perfluoro [49], and hydroxyl groups [50] were taken from the original TraPPE papers and are listed in Table 2. Parameters for unlike interactions were determined using the Lorentz-Berthelot combining rules [51,52]

$$\sigma_{ij} = (\sigma_{ii} + \sigma_{jj})/2 \quad (5)$$

$$\varepsilon_{ij} = \sqrt{\varepsilon_{ii}\varepsilon_{jj}} \quad (6)$$

United-atoms were connected with rigid bonds, for which the parameters are listed in Table S1 of the supporting information. Bond bending was governed by a harmonic potential

$$U_{bend} = k_\theta(\theta - \theta_0)^2 \quad (7)$$

where θ is the measured bond angle, θ_0 is the equilibrium bond angle, and k_θ is the force constant. Bond bending constants were taken from TraPPE [48–50], and are listed in Table S1 in supporting information. Rotations around dihedral angles were described with a cosine series

$$U_{torsion} = \sum_{i=1}^{m} c_i(1 + cos(n_i\phi - \delta_i)) \quad (8)$$

where ϕ is the dihedral angle, c_i are dihedral force constants, n is the multiplicity, and δ_i is the phase shift. Existing torsional potentials for the C–C-C–C backbone for n-alkanes and perfluoroalkanes in TraPPE were refit to use the form of Equation (8) or taken from prior work [37]. Constants for all dihedral potentials are listed in Table S2 in supplementary information.

New Fourier coefficients for torsions in $CH_3(CH_2)_5(CF_2)_2OH$ (F2H6) and $CH_3(CH_2)_6CF_2OH$ (F1H7) were optimised to reproduce rotational barriers determined from relaxed potential energy scans generated from MP2/6-31 + g(d,p) *ab initio* calculations. All *ab initio* calculations were performed in Gaussian 09 [53].

3. Calculation of solvation free energies

This section describes key details of the implementation of free energy perturbation and thermodynamic integration in GOMC. Free energy perturbation is discussed, first, followed by thermodynamic integration. Computational details for the calculations are given in Simulation Methodology.

In free energy perturbation (FEP) [23,24], the free energy difference between two states A (e.g. non-interacting solute) and state B (e.g. fully interacting solute) is given by

$$\Delta G(A \to B) = -\frac{1}{\beta}\ln\langle\exp(-\beta\Delta U_{A,B})\rangle_A \quad (9)$$

where $\Delta U_{A,B} = U_B - U_A$ is the energy difference between the system in state A and B, and $\langle\exp(-\beta\Delta U_{A,B})\rangle_A$ is the ensemble average for simulation in state A. For most systems, there is limited phase-space overlap between state A and B, leading to poor convergence of the free energy. By constructing an artificial

pathway through multistage sampling [54], satisfactory phase-space overlap can be achieved, greatly improving the accuracy and precision of the free energy calculation [55,56]. Using the multistage sampling approach, the free energy difference between two states A and B, with $N-2$ intermediate states given by [57]

$$\Delta G(A \rightarrow B) = -\frac{1}{\beta}\sum_{i=0}^{N-1} \ln \langle \exp(-\beta \Delta U_{i,i+1}) \rangle_i \quad (10)$$

where $\Delta U_{i,i+1} = U_{i+1} - U_i$ is the energy difference of the system between states i and $i+1$, and $\langle \exp(-\beta \Delta U_{i,i+1}) \rangle_i$ is the ensemble average for simulation performed in intermediate state i. A coupling parameter $0.0 \leq \lambda \leq 1.0$ is used to smoothly transform the simulated system between states A ($\lambda = 0.0$) and B ($\lambda = 1.0$), where

$$U_i = \lambda_i U_B + (1 - \lambda_i) U_A \quad (11)$$

Naive linear scaling of the intermolecular interactions with respect to λ produces a well-known numerical instability (end-point catastrophe) in the limit of $\lambda \rightarrow 0$ and $\lambda \rightarrow 1$ for Lennard-Jones potentials [58,59], which can be avoided by shifting and scaling the Lennard-Jones potential via the soft-core scheme [60,61]. Electrostatic interactions do not have the same numerical instability if a two-step transformation is applied [62], and it has been shown that it is computationally efficient to scale them linearly [63].

Therefore, in this work, soft-core scaling is used for the Lennard-Jones interactions, while linear scaling is used for the Coulombic interactions. Separate λ_{LJ} and λ_{Coul} were used to independently control the scaling of Lennard-Jones and Coulombic interactions, respectively. The energy of the solute interacting with the solvent is given by

$$U_i(r_{ij}) = \lambda_{LJ} U_{LJ}(r_{sc-ij}) + \lambda_{Coul} U_{Coul}(r_{ij}) \quad (12)$$

where

$$r_{sc-ij} = (\alpha(1 - \lambda_{LJ})^p {\sigma_{ij}}^6 + {r_{ij}}^6)^{1/6} \quad (13)$$

r_{sc-ij}, α, and p are the scaled distance, softness parameter, and soft-core power, respectively. To improve numerical convergence of the calculation, a minimum interaction diameter $\sigma_{\min} = 3.0$Å was defined for any atom with a diameter less than $\sigma_{\min}$, e.g. hydrogen atoms attached to oxygen in water or alcohols [62].

The effect of long-range corrections on predicted free energies were determined for Lennard-Jones and Coulombic interactions via a linear coupling with λ.

$$U_{LRC(LJ)} = \lambda_{LJ} \Delta U_{LRC(LJ)} \quad (14)$$

$$U_{LRC-Coul} = \lambda_{Coul}[\Delta U_{self} + \Delta U_{correction} + \Delta U_{reciprocal}] \quad (15)$$

where $\Delta U_{LRC(LJ)}$, $\Delta U_{reciprocal}$, ΔU_{self}, $\Delta U_{correction}$ are the change in the long-range correction energy due to adding a fully interacting solute to the solvent for both the Lennard-Jones and Coulombic interactions.

In thermodynamic integration, the free energy change is calculated from

$$\Delta G(A \rightarrow B) = \int_{\lambda=0}^{\lambda=1} \left\langle \frac{dU}{d\lambda} \right\rangle_\lambda d\lambda \quad (16)$$

where $dU/d\lambda$ is the derivative of energy difference with respect to λ, and $\langle dU/d\lambda \rangle_i$ is the ensemble average for a simulation run at intermediate state λ. To calculate the free energy using thermodynamic integration, the derivative of the intermolecular energy with respect to λ must be evaluated for both the Lennard-Jones and Coulombic interactions of the solute with the solvent.

$$\frac{dU_{LJ}(r_{ij})}{d\lambda_{LJ}} = U_{LJ}(r_{sc-ij}) + \frac{\lambda_{LJ} p \alpha}{6}(1 - \lambda_{LJ})^{p-1} \times \left(\frac{{\sigma_{ij}}^6}{{r_{ij}}^5}\right) F_{LJ}(r_{sc-ij}) \quad (17)$$

$$\frac{dU_{Coul}(r_{ij})}{d\lambda_{Coul}} = U_{Coul}(r_{ij}) \quad (18)$$

$$F_{LJ}(r_{ij}) = -\frac{dU_{LJ}(r_{ij})}{dr_{ij}} = \frac{4\varepsilon_{ij}}{r_{ij}}\left[12\left(\frac{\sigma_{ij}}{r_{ij}}\right)^{12} - 6\left(\frac{\sigma_{ij}}{r_{ij}}\right)^{6}\right] \quad (19)$$

The derivative of the long-range correction energies with respect to λ is given by

$$\frac{dU_{LRC(LJ)}}{d\lambda_{LJ}} = \Delta U_{LRC(LJ)} \quad (20)$$

$$\frac{dU_{LRC-Coul}}{d\lambda_{Coul}} = \Delta U_{self} + \Delta U_{correction} + \Delta U_{reciprocal} \quad (21)$$

4. Simulation methodology

4.1. Free energy calculations

The free energy calculations described in Section 3 were implemented in the development version of the open-source Monte Carlo simulation engine GOMC [45], which is available to the public via GitHub [64].

To calculate the free energy of solvation/hydration, all intermediate λ states were equilibrated independently in the canonical ensemble (NVT) for 5×10^6 Monte Carlo steps (MCS) at 298 K, followed by a 3×10^7 MCS isobaric-isothermal (NPT) ensemble simulation at 1 bar and 298 K. Production data were taken from a subsequent 5×10^7 MCS NPT simulation, which used the final configuration of the prior NPT simulation as the initial configuration. For production runs, all λ states were simulated independently in parallel. During the production run, the change in energy ($\Delta U_{i,j}$) between the current lambda state and all other lambda states, and the derivative of potential with respect to lambda ($dU_{Coul}/d\lambda_{Coul}$, $dU_{LJ}/d\lambda_{LJ}$), were evaluated and stored for post-simulation analysis every 5×10^3 MCS. A sample of GOMC free energy output is provided in Table S3. The implementation of free energy methods into GOMC was validated through calculations of free energies of solvation for various *n*-alkanes in 1-octanol. A comparison with prior calculations performed with NPT-Gibbs ensemble Monte Carlo simulations [41] is provided in Table S4, and shows that all methods produce free energies that are within 0.1 kcal/mol of each other.

To calculate the free energy of solvation in water and 1-octanol, 23 intermediate lambda states, as shown in Figure 1, were used

$$\lambda_{coul,LJ} \in \left\{ \begin{array}{c} (0.0, 0.0), (0.0, 0.05), (0.0, 0.1), (0.0, 0.15), \\ (0.0, 0.2), (0.0, 0.25), (0.0, 0.3), (0.0, 0.35), \\ (0.0, 0.4), (0.0, 0.45), (0.0, 0.5), (0.0, 0.6), \\ (0.0, 0.7), (0.0, 0.8), (0.0, 0.9), (0.0, 1.0), \\ (0.2, 1.0), (0.4, 1.0), (0.6, 1.0), (0.7, 1.0), \\ (0.8, 1.0), (0.9, 1.0), (1.0, 1.0) \end{array} \right\}$$

while 16 intermediate states were used to calculate the free energies of solvation in n-hexadecane.

$$\lambda_{coul,LJ} \in \left\{ \begin{array}{c} (0.0, 0.0), (0.0, 0.05), (0.0, 0.1), (0.0, 0.15), \\ (0.0, 0.2), (0.0, 0.25), (0.0, 0.3), (0.0, 0.35), \\ (0.0, 0.4), (0.0, 0.45), (0.0, 0.5), (0.0, 0.6), \\ (0.0, 0.7), (0.0, 0.8), (0.0, 0.9), (0.0, 1.0) \end{array} \right\}$$

While it is possible to alter the Lennard-Jones and Coulomb interactions simultaneously, recent work suggests it is more efficient to first turn on the full Lennard-Jones interactions before scaling the Coulombic interactions [63,65]. For liquid phase systems containing 1-octanol or water, the λ vectors were defined to turn on the full Lennard-Jones interaction, first, before introducing Coulombic interactions between the solute and the solvent, as shown in Figure 1, to avoid the direct interaction of atoms with 'naked' charges

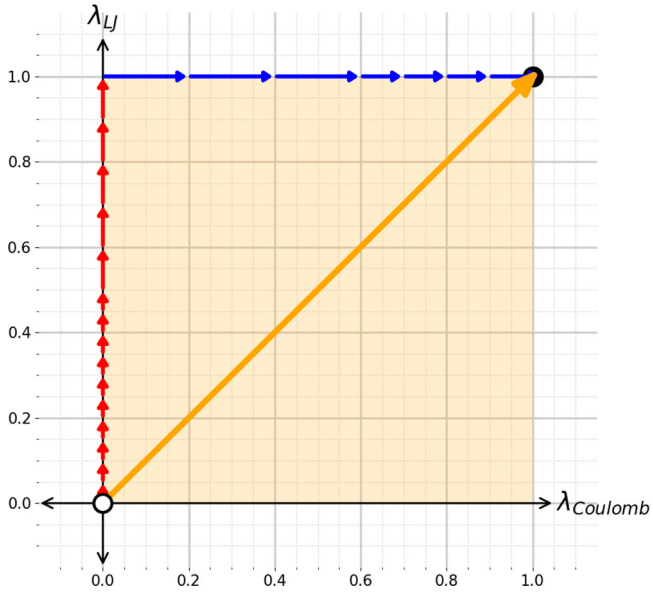

Figure 1. The transformation pathway starting from non-interacting solute (0.0, 0.0) to fully interacting solute (1.0, 1.0) in λ vector space, which is shown as an orange square on the Cartesian plane formed by the axes $\lambda_{Coulomb}$ and λ_{LJ}, which control the solute Coulombic and Lennard-Jones interactions, respectively. Intermediate states are denoted by the arrowheads.

[62,66]. The soft-core parameters used for Lennard-Jones interactions were, $\alpha = 0.5$, $p = 2$, and $\sigma_{\min} = 3.0$ [62,67].

A variety of methods were used to analyse the resulting data, including thermodynamic integration (TI) [68], Bennett acceptance ratio (BAR) [69], and multistate Bennett acceptance ratio (MBAR) [70], as implemented in the software alchemlyb [71] and alchemical-analysis [72]. A parser for GOMC output was implemented for both alchemlyb and the alchemical-analysis. Since alchemical-analysis is no longer supported by its authors, the GOMC parser for it was stored in a separate GitHub repository [73].

To determine the free energy of solvation/hydration accurately, the data points used in the calculation must be sampled at equilibrium conditions and be uncorrelated. Several techniques have been developed [74,75] to detect uncorrelated samples; both alchemlyb [71] and alchemical-analysis [72] use an autocorrelation time analysis, as implemented in pymbar [70]. In autocorrelation time analysis, the autocorrelation function $C_A(i)$ is determined for a data point i in a given data series (in this work $dU/d\lambda$), and the autocorrelation time (τ) is calculated as the integral of $C_A(i)$ [76]. Once the autocorrelation time (τ) is obtained, the gth element of the data series is treated as an uncorrelated sample, where $g = 1 + 2\tau$. In pymbar, a data point is defined

as statistically independent if $C_A(i) = 0$; however, the autocorrelation function becomes noisy as $C_A(i) \rightarrow 0$, making it difficult to rigorously determine uncorrelated samples. In practice, pymbar provides a conservative estimate of uncorrelated data, and tends to under-predict the number of uncorrelated samples.

In addition to using only uncorrelated samples, care must be taken to ensure that data used in the free energy calculation are collected from simulations that have reached equilibrium. Prior molecular dynamics simulations have shown, for example, challenges in converging liquid phase densities and free energies of solvation in 1-octanol [77]. In this work, NPT simulations of 3×10^7 MCS were used to equilibrate the system at each λ_i prior to the production run, ensuring stability of the density during free energy calculations, as shown in Figure S2 for perfluorooctanol in 1-octanol. Once free energy data were collected, convergence of the data were assessed by calculating free energies of hydration/solvation in both the forward and reverse directions with alchemical-analysis [72]. In the forward direction, the free energy was calculated using data in the order in which they were collected, while in the 'reverse' direction, the free energy was calculated from the data ordered in the reverse of which it was collected. As shown in Figure 2 for F2H6, the forward and reverse calculations match within the statistical uncertainty of the data, suggesting convergence of the free energy calculations [72,78]. Free energies were calculated from simulation data using a variety of thermodynamic integration methods (trapezoidal rule (TI) and cubic spline (TI-CUBIC)), and free energy perturbation techniques (Bennett acceptance ratio (BAR) and multi-state Bennett acceptance ratio (MBAR)). MBAR results are discussed in the body of the paper, while results for TI and BAR may be found in Table S5 of the supporting information. For simulations that have high quality sampling, and sufficient overlap between energy difference distributions, it is expected that all methods will produce similar results. As shown in Figure 3, good agreement for all intermediate states was achieved with all methods.

Additional insight is provided by the overlap matrix, as shown in Figure 4. The overlap matrix quantifies the overlap of the $\Delta U_{i,j}$ distributions between neighbouring intermediate states (i and j) and gives the probability of observing a sample from state i in state j, which can be used to detect intermediate states with insufficient overlap. In this case, the data shown in Figure 4 conform to the recommendations of Klimovich *et al.* [72]. Neighbouring states along the main diagonal have overlap values significantly above the recommended value of 0.03, indicating sufficient overlap between states has been achieved to obtain reliable free energy predictions.

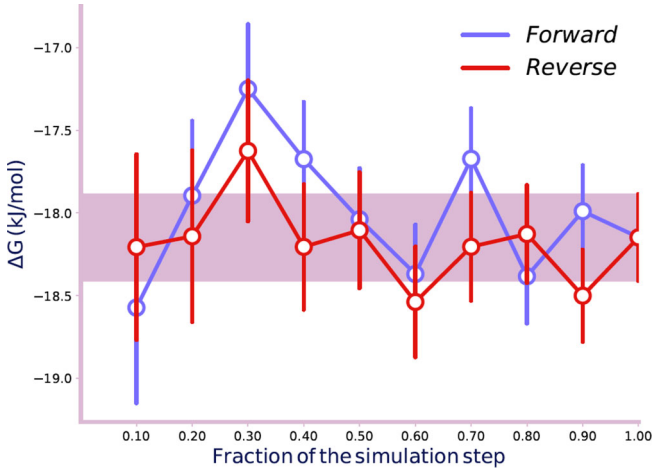

Figure 2. Solvation free energy for F2H6 in n-hexadecane plotted as a function of simulation steps. The agreement between the forward and reverse calculation is within the standard error bar (purple bar), indicating convergence of the free energy simulations.

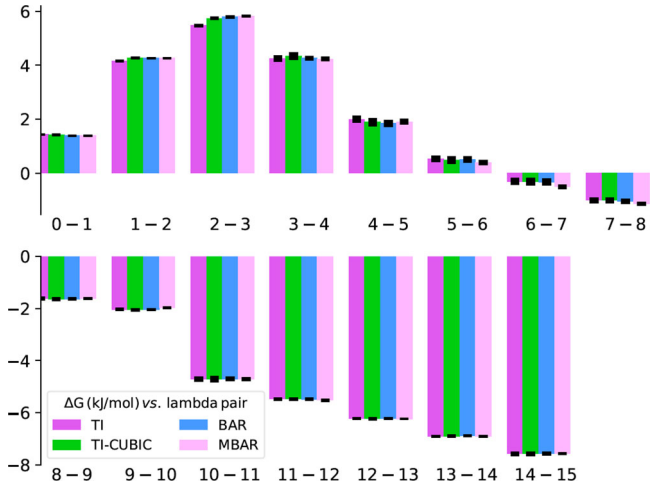

Figure 3. Intermediate free energy differences for solvation of F2H6 in n-hexadecane, calculated by a variety of thermodynamic integration and free energy perturbation techniques.

4.2. Monte Carlo simulations

NVT ensemble simulations were performed with a move ratio of 50% displacements, 20% rotations, 20% coupled-decoupled configurational-bias (CD-CBMC) regrowth [79], and 10% crankshaft [80,81]. Parameters for the configurational-bias regrowth move were 100 angle trials, 50 dihedral trials, and 10 trial locations for grown pseudo-atoms. NPT ensemble simulations were performed with similar move ratios, except for the addition of 1% volume changes, while the percentage of displacement moves was reduced to 49%. Non-bonded potentials were truncated at 14 Å [48–50] and analytical tail corrections were applied to the energy [82]. For simulations

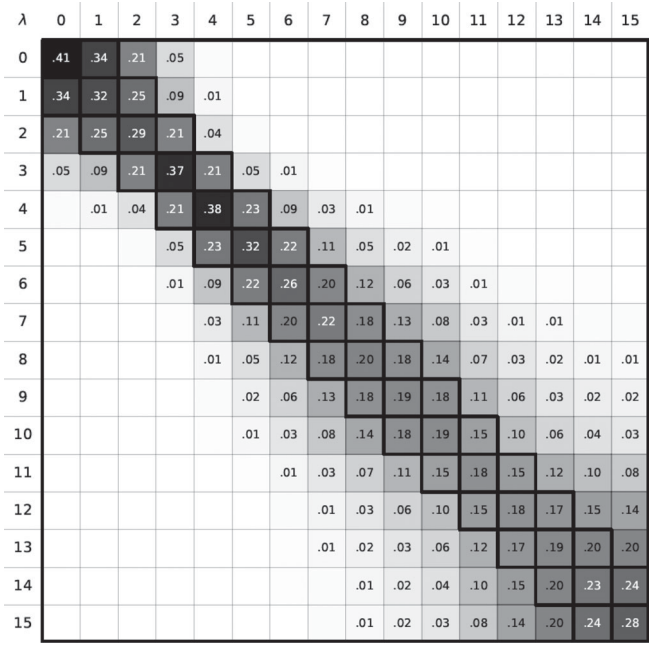

Figure 4. Overlap matrix for the solvation of F2H6 in n-hexadecane.

with electrostatic interactions, the real space part of electrostatic potential was truncated at 14 Å and an Ewald convergence tolerance of 1×10^{-5} was used [83].

During grand canonical and Gibbs ensemble Monte Carlo simulations, molecule swap moves are frequently used to sample phase-space. Intra-box swap moves may also be used to enhance the sampling of phase-space in NVT and NPT ensemble simulations. For polar molecules, where an atom has a naked charge, such as hydrogen in many alcohol and water models, during a swap move it is possible to a place opposing charges in close proximity. This produces very large negative energies that overwhelm the repulsive component of the Lennard-Jones potential, leading to the sampling of unphysical states. A common workaround is to introduce a hard inner cut-off and reject any trial moves that bring atom centres closer than 1 Å [84]. Using a hard inner cut-off in free energy simulations, however, produces incorrect sampling of the solvent structure in the limit of $\lambda \rightarrow 0$, leading to inaccurate free energies. Therefore, intra-box swap moves were not used during free energy simulations.

Liquid phase systems contained one solute in a solvent box of 200 1-octanol, 150 n-hexadecane, or 1000 water molecules. Initial cubic box sizes were selected to produce densities that were close to equilibrium, with a side length of 37.6, 41.6, and 31.3 Å for 1-octanol, n-hexadecane, and water, respectively. Initial configurations were generated with Packmol [85], and Psfgen was used to generate coordinate (*.pdb) and connectivity (*.psf) files [86].

Radial distribution functions for solute-solvent systems were determined by performing a 5×10^6 MCS equilibration in the canonical ensemble at 298 K, followed by 7×10^7 MCS NPT ensemble simulation at 1 bar and 298 K, where production data were taken from the last 5×10^7 MCS of the simulation. Atomic coordinates for all atoms in the system were stored every 2.5×10^3 MCS. Radial distribution functions were calculated from saved configurations with the gofr tool in VMD [87].

5. Results and discussion

5.1. Free energies of hydration

Free energies of hydration predicted by simulation for each solute in SPC water are listed in Table 3. From trends in the data, where $\Delta G_{water}(\mathrm{H8}) < \Delta G_{water}(H2F6) < \Delta G_{water}(H1F7) < \Delta G_{water}(F8)$, it was hypothesised that fluorination near the head group has the greatest impact on the solubility of fluorinated alcohols in water. This was confirmed through free energy calculations for two additional molecules: F1H7 and F2H6. For each of these molecules, C_α (F1H7) or C_α and C_β (F2H6) were fluorinated, while the remaining carbon atoms were CH_2 or CH_3 groups. Fluorinating C_α produces a 1.5 kcal/mol increase (less negative) in the free energy of hydration compared to 1-octanol, while fluorination of C_β and C_α produces only an additional 0.1 kcal/mol change in ΔG_{water}. This free energy change, due to fluorination of only C_α, accounts for almost half of the difference in ΔG_{water} between 1-octanol and perfluorooctanol.

Further insight into the role fluorination near the hydroxyl group plays in the altering the free energy of hydration, was obtained by calculating the separate Lennard-Jones and Coulombic contributions to the free energy for each solute, which are listed in Table 4. For solutes where C_α is hydrogenated, the Coulombic contribution to the free energy is between −6.5 and −6.1 kcal/mol, while for solutes where C_α is fluorinated, the Coulombic contribution is reduced to −5.6 to −5.4 kcal/mol. This provides evidence that fluorination of C_α reduces hydrogen bonding of the solute with water compared to 1-octanol. H1F7 and F1H7 have similar ΔG_{water} of −1.6 and −1.4 kcal/mol, respectively, which is a result of competing changes in the Lennard-Jones and Coulombic interactions. Compared to 1-octanol, fluorinating the last seven carbon atoms (H1F7), increases the Lennard-Jones contribution to ΔG_{water} by 0.9 kcal/mol, while the Coulombic interaction is decreased by 0.8 kcal/mol. Fluorinating C_α only (F1H7) results in a 1.1 kcal/mol decrease in the Coulombic contribution, with a 0.4 kcal/mol increase in the Lennard-Jones contribution to the free energy of hydration.

Table 3. Calculated free energies of hydration and solvation for alcohols predicted with the MBAR method, with a comparison to experimental data. Numbers in parenthesis correspond to the uncertainty in the last digit.

		ΔG_{C16}(kcal/mol)		$\Delta G_{1-octanol}$(kcal/mol)		ΔG_{water}(kcal/mol)		log K_{ow}	
Molecule	$\rho_{liq}(298K)$	Sim.	Exp.	Sim.	Expt.	Sim.	Expt.	Sim.	Expt.
$CH_3(CH_2)_7OH$(H8)	826(5)	−5.15(5)	−6.3 [88]	−8.6(2)	−8.13 [88]	−2.9(2)	−4.09 [89]	4.2(2)	3.0 [90]
$CF_3(CF_2)_5(CH2)_2OH$(H2F6)	1743(13)	−4.16(7) −4.16(7)	−4.0(1) [91]	−7.1(2)	−7.2(3) [91], −6.01 [92]	−1.7(2)	−0.76(3) [91], −2.01 [92], 0.50 [93]	4.0(2)	4.7(3) [21]
$CF_3(CF_2)_6CH_2OH$(H1F7)	1847(14)	−4.10(7)		−6.0(2)		−1.6(2)		3.2(2)	
$CF_3(CF_2)_7OH$(F8)	1897(15)	−3.32(7)		−5.2(2)		0.0(3)		3.8(2)	
$CH_3(CH_2)_6CF_2OH$(F1H7)	971(7)	−4.38(6)		−6.1(2)		−1.4(2)		3.4(2)	
$CH_3(CH_2)_5(CF_2)_2OH$(F2H6)	1124(7)	−4.34(6)		−5.7(2)		−1.3(2)		3.2(2)	

Table 4. Contribution of Lennard-Jones and Coulombic energy to the free energies of hydration/solvation predicted by MBAR [71]. Numbers in parenthesis correspond to the uncertainty in the last digit.

Molecule	$\Delta G_{1-octanol}$(kcal/mol)			ΔG_{water}(kcal/mol)		
	LJ	Coulomb	Total	LJ	Coulomb	Total
$CH_3(CH_2)_7OH$ (H8)	−4.84(7)	−3.8(2)	−8.6(2)	3.6(2)	−6.47(9)	−2.9(2)
$CF_3(CF_2)_5(CH2)_2OH$ (H2F6)	−3.85(7)	−3.3(2)	−7.1(2)	4.8(2)	−6.48(9)	−1.7(2)
$CF_3(CF_2)_6CH_2OH$ (H1F7)	−3.5(1)	−2.6(2)	−6.0(2)	4.4(2)	−6.08(9)	−1.6(2)
$CF_3(CF_2)_7OH$ (F8)	−3.06(9)	−2.1(1)	−5.2(2)	5.4(3)	−5.30(8)	0.0(3)
$CH_3(CH_2)_6CF_2OH$ (F1H7)	−4.15(6)	−1.9(1)	−6.1(2)	4.0(2)	−5.4(1)	−1.4(2)
$CH_3(CH_2)_5(CF_2)_2OH$ (F2H6)	−3.84(6)	−1.8(2)	−5.7(2)	4.3(2)	−5.59(9)	−1.3(2)

It should be noted that a key difference between this work and past calculations with NAMD [94] for the same molecules and models is that in this work long-range corrections for Lennard-Jones interactions are included in the free energy calculation, whereas, in past work, they were not [37]. In preliminary calculations, the contribution of long-range corrections to the free energy of hydration for these molecules was found to be approximately −1.0 to −0.8 kcal/mol, which is consistent with prior calculations for n-alkanes [95]. Accounting for this difference in the treatment of long-range corrections to the Lennard-Jones interactions brings the results shown in Table 3 in good agreement with prior calculations [37]. Inclusion of long-range corrections for the Lennard-Jones interactions substantially improves the agreement of ΔG_{water} predictions of simulation with experiment for 1-octanol, but makes agreement with the most reliable experimental data for H2F6 worse [91].

To further understand how fluorination near the head group affects the solubility of alcohols in water, radial distribution functions (RDF) were calculated for O(solute)-O(solvent) and C_α(solute)-O(solvent), and are presented in Figure 5. For all molecules, for O(solute)-O(solvent) interactions, a peak is observed at approximately 2.75 Å corresponding to hydrogen bonding between water and the solute. Peak heights varied, depending on the degree of fluorination near the hydroxyl group. Similar peak heights were observed for the O-O RDF for 1-octanol and H2F6 interacting with water, while a slightly lower peak height was observed for H1F7. The lowest peak heights were observed for perfluorooctanol, F1H7, and F2H6, which all have a fluorinated α carbon. For the C_α(solute)-O(water) radial distribution functions, perfluorooctanol, F1H7, and F2H6 all show similar behaviour with a first peak at approximately 3.9 Å, while the first peak in the RDF for 1-octanol, H1F7, and H2F6 occurs at 3.7 Å. These results for the O-O and C_α-O RDFs are consistent with prior calculations with the OPLS-AA force field [37], and show clearly that fluorination of C_α creates steric hindrance to solute-solvent hydrogen bond formation, strongly impacting on hydration free energies. These results are consistent with the work of Dalvi and Rossky, which concluded for perfluoroalkanes, that increased hydrophobicity was due to the increased volume occupied by fluorine compared to hydrogen atoms [96].

5.2. 1-octanol free energies of solvation

Free energies, predicted by the TraPPE-UA force field for each solute in 1-octanol, are listed in Table 3 and individual contributions of Lennard-Jones and Coulombic interactions to solvation free energies are listed in Table 4. Free energies of solvation for 1-octanol and H2F6 in 1-octanol were found to be in excellent agreement with experiment, with errors of 0.47 and 0.1 kcal/mol, respectively. Calculated free energies of solvation show a monotonic increase (become less negative) as fluorination of the alkyl tail increases. This is similar to the phenomena observed for hydration free energies, though fluorination of the alkyl tail has a larger impact on solvation free energies in octanol than in water, as evidenced by

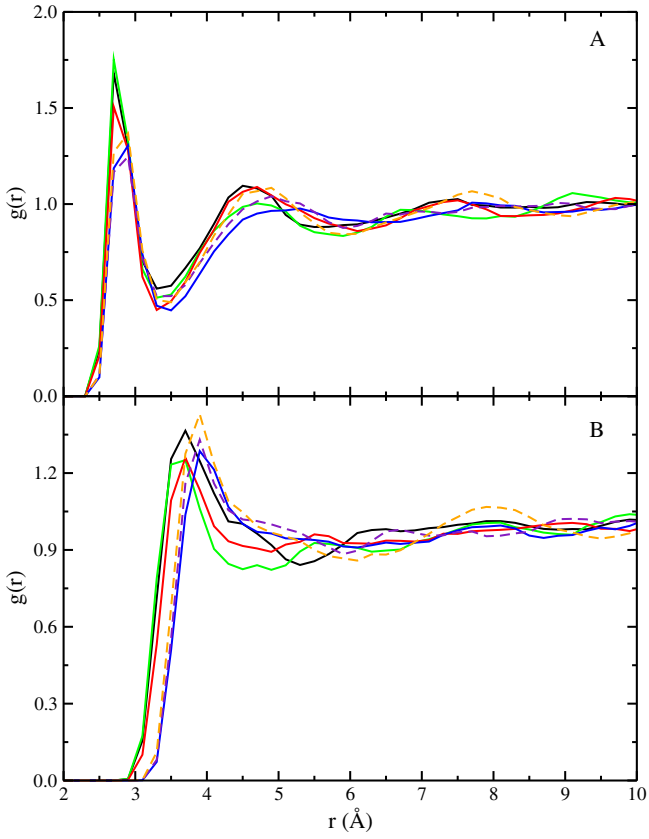

Figure 5. Radial distribution function for solute interactions with water: (A) O(solute)-O(water) and (B) C_α(solute)-O(water). Data are represented by: octanol (solid black line), H2F6 (solid green line), H1F7 (solid red line), and perfluorooctanol (solid blue line), F1H7 (dashed orange line), and F2H6 (dashed indigo line).

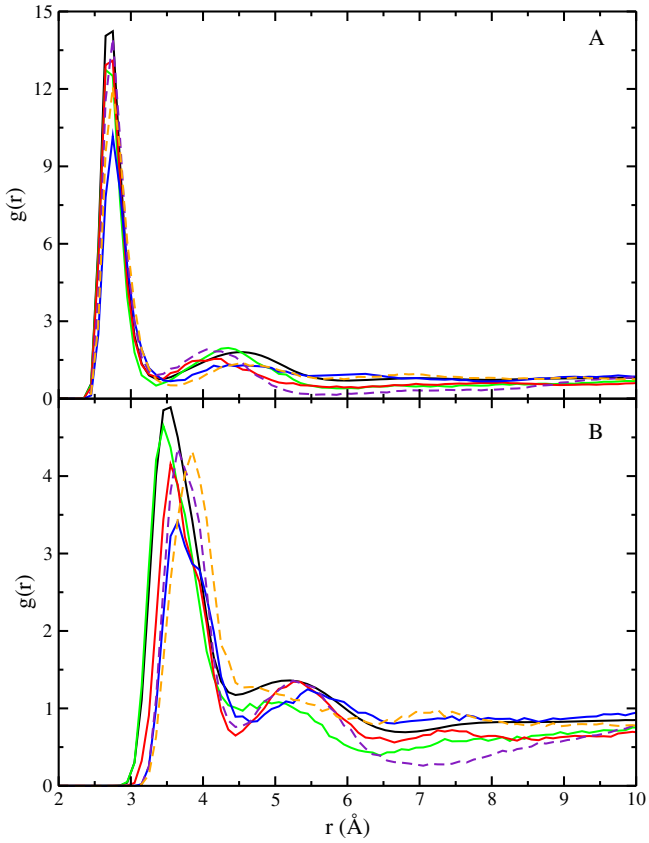

Figure 6. Radial distribution function for solute interactions with 1-octanol: (A) O(solute)-O(1-octnaol) and (B) C_α(solute)-O(1-octanol). Data are represented by: octanol (solid black line), H2F6 (solid green line), H1F7 (solid red line), and perfluorooctanol (solid blue line), F1H7 (dashed orange line), and F2H6 (dashed indigo line).

the calculated octanol–water partition coefficients for all fluorinated alcohols being lower than that of 1-octanol, despite also having lower hydration free energies.

The peak height in radial distribution functions for O(solute) with O(1-octanol), shown in Figure 6, follow a similar trend as the solvation free energies. The largest peak height was observed for 1-octanol in 1-octanol, while the lowest peak height was for perfluorooctanol. These results suggest that C_α fluorination state plays a significant role in in the predicted free energy, since fluorination near the hydroxyl group sterically hinders the solvent's ability to form hydrogen bonds with the solute. These results were confirmed by additional free energy calculations performed for F1H7 and F2H6. Fluorination of both the α and β carbons (F2H6) produces a free energy of solvation that is within 0.5 kcal/mol of perfluorooctanol, while fluorinating only the α carbon produces a free energy of solvation that is similar to H1F7.

Fluorination of C_α produced a marked decrease in the Coulombic contribution to the free energy. For F1H7, F2H6, and perfluorooctanol, the Coulombic contribution varied from -2.1 to -1.8 kcal/mol, compared to -3.8 kcal/mol for 1-octanol. Unlike solvation in water, fluorination of C_β and later carbons also impacted the hydrogen bonding of solutes with 1-octanol. Coulombic contributions to the free energy decrease with increasing fluorination, regardless of position on the alkyl tail; for H2F6 $\Delta G_{Coul} = -3.3$ kcal/mol, while for H1F7 $\Delta G_{Coul} = -2.6$ kcal/mol. Radial distribution functions for C_α(solute)-O(solvent) interactions show decreased height of the first peak going from 1-octanol to H2F6 and H1F7. While both water and 1-octanol form complex hydrogen bonded networks, the alkyl tail of 1-octanol creates additional constraints on the microstructures that may form. Adding bulky fluorine atoms to the alkyl tail of solutes, beyond C_α and C_β, appears to be capable of creating steric hindrance to hydrogen bond formation between the solute and the 1-octanol solvent.

5.3. n-hexadecane free energies of solvation

The air-hexadecane partition coefficient provides a measurement of non-specific interactions between molecules and plays an important role as a compound descriptor used in linear solvation energy relationships (LSER). LSER models are used for prediction of solute partitioning in a variety of process, providing data that are needed for transport and environmental fate modelling [97,98]. Additionally, water-hexadecane partition coefficients are used to model lipophilic systems, such as the core of lipid bilayers [99,100]. Predicting solvation free energies of fluorinated 1-octanol analogues in n-hexadecane provides additional insight into the role of fluorine in altering Lennard-Jones interactions between the solute and organic solvents, without the complications of hydrogen bonding present in the solvent 1-octanol.

Free energies predicted by the TraPPE-UA force field for each solute in n-hexadecane are listed in Table 3. Experimental data for these compounds is limited to 1-octanol and H2F6. For H2F6, simulations predicted $\Delta G_{C16} = -4.16$ kcal/mol, which is in close agreement with the experimental value of -4.0 kcal/mol from Goss *et al.* [91]. For 1-octanol, simulations predict $\Delta G_{C16} = -5.15$ kcal/mol vs. the experimental value of -6.3 kcal/mol.

Interestingly, the data follow the same trend with increasing fluorination as the free energies of hydration ($\Delta G_{C16}(\mathrm{H8}) < \Delta G_{C16}(H2F6) < \Delta G_{C16}(H1F7) < \Delta G_{C16}(F8)$), despite the absence of specific hydrogen bonding interactions. Fluorinating only C_α (F1H7) produces a 0.77 kcal/mol increase in the free energy of solvation compared to 1-octanol, while fluorination of C_β and C_α (F2H6) produces only an additional 0.04 kcal/mol change in ΔG_{C16}. The free energy change due to fluorination of only C_α accounts for almost half of the difference in ΔG_{C16} between 1-octanol and perfluorooctanol. Fluorination of C_β and later carbons (H2F6) produces only an additional 0.18 kcal/mol change in ΔG_{C16}, as compared to F2H6.

Radial distribution functions for each solute interacting with n-hexadecane are presented in Figure 7. For O(solute)-CH_x(n-hexadecane), 1-octanol and H2F6 have similar behaviour, while, for all other solutes, the first peak is slightly lower and shifted to larger distances, illustrating the additional space occupied by the fluorine atoms near the hydroxyl group. For the CH_x or CF_x(solute)-CH_x(n-hexadecane) radial distribution functions, the most highly fluorinated molecules, H1F7 and perfluorooctanol, display similar behaviour, while a reduction in the number of fluorine atoms (i.e. F1H7 and F2H6), causes the first peak in the RDF to shift to smaller distances.

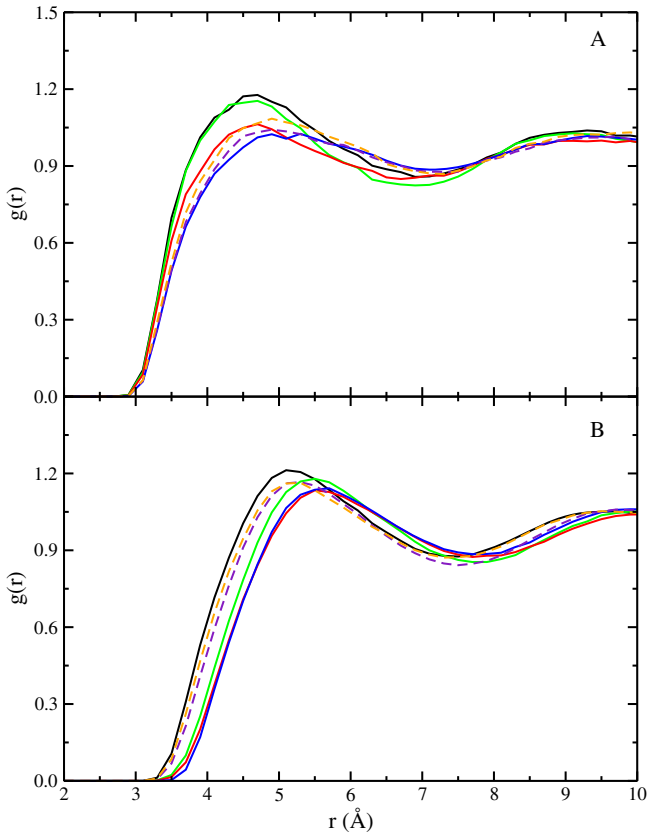

Figure 7. Radial distribution function for solute interactions with n-hexadecane: (A) interaction of O(solute)-CH_x(n-hexadecane) and (B) CH_x or CF_x(solute)-CH_x(n-hexadecane). Data are represented by: octanol (solid black line), H2F6 (solid green line), H1F7 (solid red line), and perfluorooctanol (solid blue line), F1H7 (dashed orange line), and F2H6 (dashed indigo line).

6. Conclusions

In this work, free energies of solvation in water, 1-octanol, and n-hexadecane were calculated with Monte Carlo simulations in the isobaric-isothermal ensemble for a variety of fluorinated analogues of 1-octanol. The combination of SPC water and TraPPE-UA were found to provide a good qualitative reproduction of experimental data.

Davli and Rossky concluded that the molecular basis for hydrophobicity exhibited by perfluoroalkanes was due to the larger volume occupied by fluorine compared to hydrogen atoms [96]. Similarly, this work has shown that the larger volume of fluorine atoms compared to hydrogen leads to the oleophobic behaviour of fluoroalcohols. Fluorination of the α and β carbons was found to have the greatest impact on the free energy of hydration and the free energy of solvation in 1-octanol. The addition of fluorine atoms to the alpha and beta carbons creates a steric hindrance to hydrogen bonding between the solute and the solvent. In 1-octanol and n-hexadecane, subtle effects of fluorination of methyl groups further

away from the hydroxyl group on hydrogen bonding were observed. Down-chain fluorination increases the volume occupied by the solute, while intramolecular geometrical constraints and barriers to dihedral rotation limit the ability of 1-octanol to reorient to form hydrogen bonds with the solute. In n-hexadecane, reductions in the free energy of solvation with fluorination are largely due to increases volume occupied by fluorine atoms and their lower energy density.

Acknowledgements

Some of the computations in this work were performed with resources from the Grid Computing initiative at Wayne State University.

Disclosure statement

No potential conflict of interest was reported by the authors.

Funding

Funding from the National Science Foundation OAC-1642406 (Division of Advanced Cyberinfrastructure) is gratefully acknowledged.

ORCID

Jeffrey J. Potoff http://orcid.org/0000-0002-4421-8787

References

[1] K. Shinoda, M. Hato, and T. Hayashi, J. Phys. Chem. **76** (6), 909 (1972).
[2] M.K. Bernett and W.A. Zisman, J. Phys. Chem. **63** (11), 1911 (1959).
[3] H. M. Scholberg, R.A. Guenthner, and R.I. Coon, J. Phys. Chem. **57** (9), 923 (1954).
[4] P. Thomas, Surf. Coat. Int. **81** (12), 604 (1998).
[5] X. Trier, K. Granby, and J.H. Christensen, Environ. Sci. Pollut. R. **18** (7), 1108 (2011).
[6] C.A. Moody and J.A. Field, Environ. Sci. Technol. **34** (18), 3864 (2000).
[7] K. Prevedouros, I.T. Cousins, R.C. Buck, and S.H. Korzeniowski, Environ. Sci. Technol. **40** (1), 32 (2006).
[8] J.S.C. Liou, B. Szostek, C.M. DeRito, and E.L. Madsen, Chemosphere **80** (2), 176 (2010).
[9] J.W. Martin, M.M. Smithwick, B.M. Braune, P.F. Hoekstra, D.C.G. Muir, and S.A. Mabury, Environ. Sci. Technol. **38** (2), 373 (2004).
[10] B.D. Key, R.D. Howell, and C.S. Criddle, Environ. Sci. Technol. **31** (9), 2445 (1997).
[11] M. Scheringer, X. Trier, I.T. Cousins, P. de Voogt, T. Fletcher, Z.Y. Wang, and T.F. Webster, Chemosphere **114**, 337 (2014).
[12] G. Kostov, F. Boschet, and B. Ameduri, J. Fluorine Chem. **130** (12), 1192 (2009).
[13] A. Drame, E.T. de Givenchy, S.Y. Dieng, S. Amigoni, M. Oumar, A. Diouf, T. Darmanin, and F. Guittard, Langmuir **29** (48), 14815 (2013).
[14] L.A. D'Agostino and S.A. Mabury, Environ. Sci. Technol. **48** (1), 121 (2014).
[15] B.J. Place and J.A. Field, Environ. Sci. Technol. **46** (13), 7120 (2012).
[16] F. Wania and D. Mackay, Sci. Total Environ. **160–61**, 211 (1995).
[17] Estimation Programs Interface Suite™ for Microsoft® Windows (United States Environmental Protection Agency, Washington, DC, USA, 2012).
[18] A.J. Leo, CLOGP (Daylight Chemical Information Systems, Irvine, CA, 1991).
[19] S.H. Hilal, S.W. Karickhoff, and L.A. Carreira, QSAR Comb. Sci. **23** (9), 709 (2004).
[20] F. Eckert and A. Klamt, AIChE J. **48** (2), 369 (2002).
[21] H.P.H. Arp, C. Niederer, and K.U. Goss, Environ. Sci. Technol. **40** (23), 7298 (2006).
[22] T.P. Straatsma and J.A. Mccammon, Annu. Rev. Phys. Chem. **43**, 407 (1992).
[23] R.W. Zwanzig, J. Chem. Phys. **23** (10), 1915 (1955).
[24] R.W. Zwanzig, J. Chem. Phys. **22** (8), 1420 (1954).
[25] E. Darve and A. Pohorille, J. Chem. Phys. **115** (20), 9169 (2001).
[26] D. Rodriguez-Gomez, E. Darve, and A. Pohorille, J. Chem. Phys. **120** (8), 3563 (2004).
[27] D.L. Mobley, K.L. Wymer, N.M. Lim, and J.P. Guthrie, J. Comput. Aided Mol. Des. **28** (3), 135 (2014).
[28] C.C. Bannan, K.H. Burley, M. Chiu, M.R. Shirts, M.K. Gilson, and D.L. Mobley, J. Comput. Aided Mol. Des. **30** (11), 927 (2016).
[29] D.L. Mobley, C.I. Bayly, M.D. Cooper, and K.A. Dill, J. Phys. Chem. B **113** (14), 4533 (2009).
[30] D.L. Mobley, C.I. Bayly, M.D. Cooper, M.R. Shirts, and K.A. Dill, J. Chem. Theory Comput. **5** (2), 350 (2009).
[31] J.D. Chodera, D.L. Mobley, M.R. Shirts, R.W. Dixon, K. Branson, and V.S. Pande, Curr. Opin. Struct. Biol. **21** (2), 150 (2011).
[32] W.L. Jorgensen, Acc. Chem. Res. **42** (6), 724 (2009).
[33] W.L. Jorgensen, Science. **303** (5665), 1813 (2004).
[34] N. Bhatnagar, G. Kamath, and J.J. Potoff, Phys. Chem. Chem. Phys. **15** (17), 6467 (2013).
[35] A. Ahmed and S.I. Sandler, J. Chem. Theory Comput. **9** (6), 2774 (2013).
[36] G. Kamath, N. Bhatnagar, G.A. Baker, S.N. Baker, and J.J. Potoff, Phys. Chem. Chem. Phys. **14** (13), 4339 (2012).
[37] W. Zygmunt and J.J. Potoff, Fluid Phase Equilibr. 407, 314 (2016).
[38] P.V. Klimovich and D.L. Mobley, J. Comput. Aided Mol. Des. **24** (4), 307 (2010).
[39] M.G. Martin and J.I. Siepmann, J. Am. Chem. Soc. **119** (38), 8921 (1997).
[40] B. Chen and J.I. Siepmann, J. Am. Chem. Soc. **122** (27), 6464 (2000).
[41] M.S. Barhaghi and J.J. Potoff, Fluid Phase Equilibr. 486, 106 (2019).
[42] A. Poursaeidesfahani, A. Torres-Knoop, D. Dubbeldam, and T.J.H. Vlugt, J. Chem. Theory Comput. **12** (4), 1481 (2016).
[43] M.S. Barhaghi, K. Torabi, Y. Nejahi, L. Schwiebert, and J.J. Potoff, J. Chem. Phys. **149** (7), 072318 (2018).
[44] N. Rai, D. Bhatt, J.I. Siepmann, and L.E. Fried, J. Chem. Phys. **129** (19), 194510 (2008).

[45] Y. Nejahi, M.S. Barhaghi, J. Mick, B. Jackman, K. Rushaidat, Y.Z. Li, L. Schwiebert, and J. Potoff, Softwarex 9, 20 (2019).
[46] N.L. Stock, D.A. Ellis, L. Deleebeeck, D.C.G. Muir, and S.A. Mabury, Environ. Sci. Technol. **38** (6), 1693 (2004).
[47] H.J.C. Berendsen, J.P.M. Postma, W.F. Van Gunsteren, and J. Hermans, *Intermolecular Forces*, edited by B. Pullman (Reidel, Dordrecht, 1981).
[48] M.G. Martin and J.I. Siepmann, J. Phys. Chem. B **102** (14), 2569 (1998).
[49] L. Zhang and J.I. Siepmann, J. Phys. Chem. B **109** (7), 2911 (2005).
[50] B. Chen, J.J. Potoff, and J.I. Siepmann, J. Phys. Chem. B **105** (15), 3093 (2001).
[51] H.A. Lorentz, Ann. Phys. **248** (1), 127 (1881).
[52] D. Berthelot, C. R. Hebd. Seanc. Acad. Sci. (Paris) **126**, 1703 (1898).
[53] M.J. Frisch, G.W. Trucks, H.B. Schlegel, G.E. Scuseria, M.A. Robb, J.R. Cheeseman, G. Scalmani, V. Barone, B. Mennucci, G.A. Petersson, H. Nakatsuji, M. Caricato, X. Li, H.P. Hratchian, A.F. Izmaylov, J. Bloino, G. Zheng, J.L. Sonnenberg, M. Hada, M. Ehara, K. Toyota, R. Fukuda, J. Hasegawa, M. Ishida, T. Nakajima, Y. Honda, O. Kitao, H. Nakai, T. Vreven, J.A. Montgomery Jr., J.E. Peralta, F. Ogliaro, M. Bearpark, J.J. Heyd, E. Brothers, K.N. Kudin, V.N. Staroverov, R. Kobayashi, J. Normand, K. Raghavachari, A. Rendell, J.C. Burant, S.S. Iyengar, J. Tomasi, M. Cossi, N. Rega, J.M. Millam, M. Klene, J.E. Knox, J.B. Cross, V. Bakken, C. Adamo, J. Jaramillo, R. Gomperts, R.E. Stratmann, O. Yazyev, A.J. Austin, R. Cammi, C. Pomelli, J.W. Ochterski, R.L. Martin, K. Morokuma, V.G. Zakrzewski, G.A. Voth, P. Salvador, J.J. Dannenberg, S. Dapprich, A.D. Daniels, Ö. Farkas, J.B. Foresman, J.V. Ortiz, J. Cioslowski, and D.J. Fox, Gaussian 09, Revision A.02 (Gaussian Inc, Wallingford, CT, 2009).
[54] J.P. Valleau and D.N. Card, J. Chem. Phys. **57** (12), 5457 (1972).
[55] D. Wu and D.A. Kofke, J. Chem. Phys. **123** (8), 084109 (2005).
[56] D. Wu and D.A. Kofke, J. Chem. Phys. **123** (5), 054103 (2005).
[57] A. Pohorille, C. Jarzynski, and C. Chipot, J. Phys. Chem. B **114** (32), 10235 (2010).
[58] D.L. Beveridge and F.M. Dicapua, Annu. Rev. Biophys. Bio. 18, 431 (1989).
[59] T. Simonson, Mol. Phys. **80** (2), 441 (1993).
[60] T.C. Beutler, A.E. Mark, R.C. Vanschaik, P.R. Gerber, and W.F. Vangunsteren, Chem. Phys. Lett. **222** (6), 529 (1994).
[61] M. Zacharias, T.P. Straatsma, and J.A. Mccammon, J. Chem. Phys. **100** (12), 9025 (1994).
[62] T. Steinbrecher, I. Joung, and D.A. Case, J. Comput. Chem. **32** (15), 3253 (2011).
[63] L.N. Naden and M.R. Shirts, J. Chem. Theory Comput. **11** (6), 2536 (2015).
[64] Y. Nejahi, M.S. Barhaghi, J. Mick, B. Jackman, K. Rushaidat, Y.Z. Li, L. Schwiebert, and J. Potoff, GOMC: GPU Optimized Monte Carlo (https://github.com/GOMC-WSU/, 2019).
[65] L.N. Naden, T.T. Pham, and M.R. Shirts, J. Chem. Theory Comput. **10** (3), 1128 (2014).
[66] J. Anwar and D.M. Heyes, J. Chem. Phys. **122** (22), 224117 (2005).
[67] J.W. Pitera and W.F. van Gunsteren, J. Phys. Chem. B **105** (45), 11264 (2001).
[68] H. Paliwal and M.R. Shirts, J. Chem. Theory Comput. **7** (12), 4115 (2011).
[69] C.H. Bennett, J. Comput. Phys. **22** (2), 245 (1976).
[70] M.R. Shirts and J.D. Chodera, J. Chem. Phys. **129** (12), 124105 (2008).
[71] I. Kenney, D. Dotson, and O. Beckstein, alchemistry/alchemlyb: Release 0.1.0 (https://doi.org/10.5281/zenodo.583647, 2017).
[72] P.V. Klimovich, M.R. Shirts, and D.L. Mobley, J. Comput. Aided Mol. Des. **29** (5), 397 (2015).
[73] P.V. Klimovich, M.R. Shirts, and D.L. Mobley, alchemical-analysis (https://github.com/msoroush/alchemical-analysis, 2015).
[74] T.P. Straatsma, H.J.C. Berendsen, and J.P.M. Postma, J. Chem. Phys. **85** (11), 6720 (1986).
[75] H. Flyvbjerg and H.G. Petersen, J. Chem. Phys. **91** (1), 461 (1989).
[76] J.D. Chodera, W.C. Swope, J.W. Pitera, C. Seok, and K.A. Dill, J. Chem. Theory Comput. **3** (1), 26 (2007).
[77] C.C. Bannan, G. Calabro, D.Y. Kyu, and D.L. Mobley, J. Chem. Theory Comput. **12** (8), 4015 (2016).
[78] P. Liu, F. Dehez, W.S. Cai, and C. Chipot, J. Chem. Theory Comput. **8** (8), 2606 (2012).
[79] M.G. Martin and J.I. Siepmann, J. Phys. Chem. B **103** (21), 4508 (1999).
[80] A. Baumgartner and K. Binder, J. Chem. Phys. **71** (6), 2541 (1979).
[81] A.J. Pertsin, J. Hahn, and H.P. Grossmann, J. Comput. Chem. **15** (10), 1121 (1994).
[82] J.R. Mick, M.S. Barhaghi, B. Jackman, L. Schwiebert, and J.J. Potoff, J. Chem. Eng. Data **62** (6), 1806 (2017).
[83] D. Fincham, Mol. Simulat. **13** (1), 1 (1994).
[84] J.A. Barker and R.O. Watts, Chem. Phys. Lett. **3** (3), 144 (1969).
[85] L. Martinez, R. Andrade, E.G. Birgin, and J.M. Martinez, J. Comput. Chem. **30** (13), 2157 (2009).
[86] W. Humphrey, A. Dalke, and K. Schulten, J. Mol. Graph. Model. **14** (1), 33 (1996).
[87] B.G. Levine, J.E. Stone, and A. Kohlmeyer, J. Comput. Phys. **230** (9), 3556 (2011).
[88] J.B. Li, T.H. Zhu, G.D. Hawkins, P. Winget, D.A. Liotard, C.J. Cramer, and D.G. Truhlar, Theor. Chem. Acc. **103** (1), 9 (1999).
[89] C.P. Kelly, C.J. Cramer, and D.G. Truhlar, J. Chem. Theory Comput. **1** (6), 1133 (2005).
[90] C. Curutchet, M. Orozco, and F.J. Luque, J. Comput. Chem. **22** (11), 1180 (2001).
[91] K.U. Goss, G. Bronner, T. Harner, H. Monika, and T.C. Schmidt, Environ. Sci. Technol. **40** (11), 3572 (2006).
[92] Y.D. Lei, F. Wania, D. Mathers, and S.A. Mabury, J. Chem. Eng. Data **49**, 1013 (2004).
[93] Y.X. Wu and V.W.C. Chang, J. Chem. Eng. Data **56** (8), 3442 (2011).
[94] J.C. Phillips, R. Braun, W. Wang, J. Gumbart, E. Tajkhorshid, E. Villa, C. Chipot, R.D. Skeel, L. Kale, and K. Schulten, J. Comput. Chem. **26** (16), 1781 (2005).

[95] J.T. Wescott, L.R. Fisher, and S. Hanna, J. Chem. Phys. **116** (6), 2361 (2002).
[96] V.H. Dalvi and P.J. Rossky, Proc. Natl. Acad. Sci. U.S.A. **107** (31), 13603 (2010).
[97] G. Bronner, K. Fenner, and K.U. Goss, Fluid Phase Equilibr. 299 (2), 207 (2010).
[98] A. Stenzel, S. Endo, and K.U. Goss, J. Chromatogr. A. **1220**, 132 (2012).
[99] N.P. Franks and W.R. Lieb, Nature **274** (5669), 339 (1978).
[100] A. Finkelstein, J. Gen. Physiol. **68** (2), 127 (1976).